6

CVD diamond sensors

In this Chapter general properties of CVD diamond are introduced. Characterisation using radioactive sources is presented and the charge-carrier lifetime is determined for our sCVD diamond sample. Tests using electron beam were performed at PHIL and dependence of the signal on the beam intensity is shown.

6.1 Properties of CVD diamond

Diamond is a metastable allotrope of carbon, it has a face-centered cubic structure [98] (see Fig. 6.1 (a)) formed by the carbon atoms in a covalent network lattice (sp^3 [1]) and it is known as the hardest bulk material with highest thermal conductivity. The diamond manufactured using "chemical vapour deposition"(CVD) method is usually called CVD diamond. CVD diamond technology was discovered in the 1950s, after the high pressure and high temperatures (HPHT) diamond growth technique, which was commonly used to convert graphite into diamond.

6.1.1 CVD process

Different from the HPHT method, the CVD process uses gas-phase chemical reactions above a solid surface to grow the diamond. Under normal conditions, the thermodynamically stable crystalline phase of carbon is graphite rather than diamond. Hence, the main requirement of diamond CVD is to deposit carbon and simultaneously suppress

[1] A mixed hybridization state formed by one s-orbital and three p-orbitals, namely p_x, p_y and p_z. Diamond consists purely of sp^3 hybridized bonds. (see Ref. [99]).

the formation of graphitic sp^2-bonds [1] [100].The simplified diamond growth conditions for microwave plasma assisted CVD are shown in Fig. 6.1 (b). A mixture of hydrogen (>90 %) and methane gas is activated in microwave plasma, methane is used as Carbon supply and hydrogen molecules are dissociated into atomic hydrogen. A high supersaturation of atomic hydrogen can not only break up double bonds thus converting graphite bonds into diamond bonds, but also etch graphite from the surface, prevent the built up of polymers and keep the diamond lattice stable by termination of the surface. Typical deposition conditions are: 1% methane in hydrogen as source gas, 700-1000°C deposition temperature and gas pressures in the range 30-300 Torr (i.e. 4-40 kPa) [101].

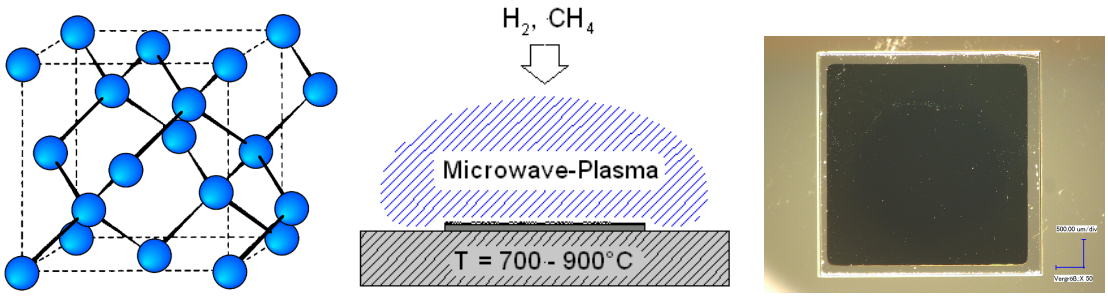

(a) (b) (c)

Figure 6.1: (a): Face-centered cubic structure of diamond; (b): CVD diamond growth conditions (picture from [100]); (c): A sCVD diamond pad sample (4.5mm×4.5mm × 500μm) with Al metallisation (4.11mm× 4.11 mm).

6.1.2 CVD diamond classification

Depending on the substrate used for diamond deposition, the CVD diamond can be divided into two groups: single crystalline (sCVD) diamond and polycrystalline CVD (pCVD) diamond.

For the growth of sCVD diamond, surface-treated HPHT diamond crystal is usually used as substrate. In this case new carbon atoms are added to the existing diamond lattice. Therefore the size of sCVD diamond depends mainly on the size of the seeds, and the availability of large area seed crystals is very limited and costly. The restricted

[1] The sp^2-hybridization is the combination of one s-orbitals with only two p-orbitals, namely p_x and p_y. Graphite consists purely of sp^2 hybridized bonds [99]

size of the HPHT seeds is about 4.5×4.5 mm^2. The sCVD diamond is separated from the HPHT substrate after the growth by a laser-cutting technique and polished to the desired thickness [102]. Free-standing diamond membranes mounted on a silicon support have been demonstrated with thicknesses as low as 30 nm. On the other end of the scale diamond disks with more than 2 mm thickness are commercially available [100]. The typical dimension of a sCVD diamond is 4.5×4.5×0.5 mm^3 as the samples used in our experiments (see Fig. 6.1 (c)).

For the growth of pCVD diamond, non-diamond substrates can be used with pre-treatment of the surface to allow diamond formation. E.g. by polishing a silicon substrate with diamond powder tiny diamond particles remain on the surface that act as seeds for the growth of small diamond crystals. During deposition the size of these crystals increases until they form a continuous compact layer of small diamond crystals. This allows pCVD diamond to form as large area disks or coatings.

Although pCVD diamond can be formed in larger area than sCVD diamond, they contains many grain-boundaries which act as charge trapping centers for free charge carriers and consequently lead to a decreased charge collection distance. Therefore, the electric properties of pCVD diamond is less favorable comparing with sCVD diamond.

6.1.3 Advantages of using CVD diamond

Comparing with other types of semiconductor detector such as silicon detector, detector based on CVD diamond has the following advantages:

- Optimal band gap: the band gap of diamond is 5.5 eV compared with 1.1 eV for silicon. This result in a lower noise level and a quasi negligible leakage current. On the other hand, also due to the larger band gap, the average energy required to liberate an e-h pair in diamond is 13.1 eV, 3.6 times larger than for silicon (3.6 eV), resulting in a smaller signal. However, the overall signal to noise ratio (SNR) is slightly higher for diamond than for silicon as reported in Ref. [103]. In Ref. [104] it was also pointed out that the optimal band gap for large SNR is around 6 eV.
- High mobility: the signal pulse width depends on the mobility of the charge carriers: high mobility leads to short pulses. The charge carrier mobility depends on the purity of the diamond and the published values for CVD diamond varies

from 1300 to 4500 $cm^2 \cdot V^{-1} \cdot s^{-1}$ for electrons and from 2050 to 3800 $cm^2 \cdot V^{-1} \cdot s^{-1}$ for holes [102]. The typical pulse width from a sCVD diamond sensor is at several ns level which enables fast enough data acquisition for 100 MHz bunch frequency.

- High radiation hardness: diamond is radiation hard up to several MGy of photons and electrons, up to 10^{15} (neutrons and high energetic protons)/cm^2 and $> 10^{15}$ pions /cm^2 [105]. In such conditions, leakage current remains negligible and charge collection distance (see section 6.1.5) decreases only slightly. Hence, diamond is considered as an ideal material for particle detectors in harsh radiation environment.
- High breakdown field: the breakdown field denotes the maximal field strength the material can withstand intrinsically without breaking down. Diamond has a much higher breakdown field of 1000 $V \cdot \mu m^{-1}$ than that of silicon (30 $V \cdot \mu m^{-1}$).
- Large thermal conductivity: the thermal conductivity of diamond was measured to be about 2000 W/m·K, which is about 5 times higher than that of copper [106].

Table 6.1 shows the general properties of sCVD diamond compared with silicon in normal conditions.

6.1.4 Energy deposition of electrons in diamond

Low energy electrons passing through diamond deposit energy mainly by ionization (collision) processes while high energy electrons (>10 MeV) loose energy mainly due to bremsstrahlung (radiation) processes. The particles with energy loss rates close to the minimum are called minimum ionizing particles (MIP), and all particles with energies above the MIP energy are considered as approximately minimum ionizing in solid state detectors [109]. The mean energy loss (stopping power) due to ionization can be calculated from the Bethe-Bloch formula [110]. The left plot in Fig. 6.2 shows the stopping powers as a function of energy of incident electrons. It can be seen that the MIP energy of electrons is around 1.6 MeV. Simulations were done in GEANT4 to get the distribution of deposited energy by the MIPs inside a 500 μm diamond. The simulated result is displayed in the right plot of Fig. 6.2. This distribution is well fitted

Property	Diamond	Silicon
Atomic number	6	14
Density, [g· cm^{-3}]	3.5	2.32
Band gap, [eV]	5.5	1.1
Resistivity, [Ω·cm]	$> 10^{12}$	10^5
Breakdown field, [V·μm^{-1}]	1000 [107]	30 [108]
Electron mobility, [cm^2· V^{-1}· s^{-1}]	1300∼4500	1500
Hole mobility, [cm^2· V^{-1}· s^{-1}]	2050∼3800	500
Electron saturation velocity, [μm·ns^{-1}]	141	100
Hole saturation velocity, [μm·ns^{-1}]	96	100
Dielectric constant	5.6	11.7
Energy per e-h pair, [eV]	13∼16 [111]	3.6
Av.min.ionizing signal per 100 m	3600	8000

Table 6.1: General properties of sCVD diamond compared with silicon in normal conditions

to a Landau distribution, which is used to describe the energy spectrum observed in thin layers.

The Most Probable Value (MPV) fitted from the Landau distribution gives an energy loss of 245.9±0.1 keV for 500 μm diamond, which corresponds to 4.92 MeV/cm of energy loss. The calculated mean energy loss from the Bethe-Bloch formula is around 5.5 MeV/cm. As the energy required to create an electron-hole pair in diamond is reported to be 13 eV to 16 eV [111], and the average number of electron hole pairs per minimum ionizing particles per 100 μm is 3600 [112], the mean energy loss should be 4.68∼ 5.76 MeV/cm. Our calculated and simulated values are close to this range.

6.1.5 Charge collection process and charge collection distance

Charge collection process

According to the Shockley-Ramo theorem [113, 114], the instantaneous current i induced on a given electrode due to the motion of a charge is given by:

$$i = E_v q v \tag{6.1}$$

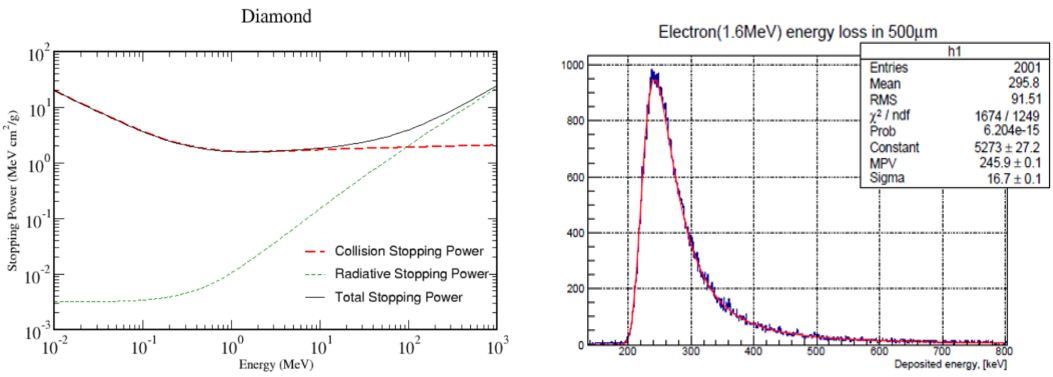

Figure 6.2: Left: the mean energy loss of an electron in diamond; Right: Landau distribution simulated using Geant4

where q is the charge of the particle;v is its instantaneous velocity, and E_v is the component of the electric field in the direction of v at the charge's instantaneous position, under the following conditions: charge removed, given electrode raised to unit potential, and all other conductors grounded.

When the particles go through the diamond, the electron-hole pairs are generated due to the ionization processes. If a bias voltage is applied to the electrodes on the surfaces of the diamond, then an electric field is formed in the bulk of diamond. Under the force of this electric field, the electrons and holes start to move and this movement induces the current on the electrodes as described by the Shockley-Ramo theorem. Once the charge-carriers have arrived at the electrodes, the signals are "over" [115].

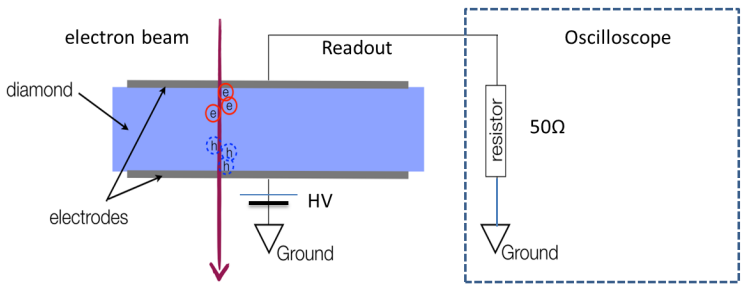

Figure 6.3: Charge generation and collection scheme

Charge collection distance

During the charge collection process, the electrons and holes have a certain probability to get trapped or recombined due to different kind of defects inside the diamond bulk. Among all the defects, the grain boundaries are suspected to be charge trapping and recombination centers [102, 116]. Neglecting border limits, the sum of the mean free paths for electrons and holes gives the overall average distance that electrons and holes drift apart in an electric field. This value has been established as the charge collection distance [109] .

The charge collection distance (d_c) is considered as a common figure of merit to characterise the manufacture quality of a diamond, especially for the pCVD diamond, the d_c of which is usually much less than the thickness of the diamond (d). However, for the sCVD diamond, the d_c can sometimes be equal to or even greater than the thickness of the diamond.

As the average minimum-ionizing particle generates about 3600 electron-hole pairs in each 100 μm of diamond, the total charge generated (Q_{gen}) can be calculated as Q_{gen}= 36×d, where d is in μm scale.

If the electrons and holes get trapped or recombined after separating by the distance d_c, then the charge collected by the electrodes (Q_{coll}) can be expressed as:

$$Q_{coll} = Q_{gen} \times \frac{d_c}{d} \tag{6.2}$$

Knowing the charge collected, the charge collection distance can be calculated as:

$$d_c = \frac{Q_{coll}}{36\ e^-/\mu m} \tag{6.3}$$

The ratio between the total generated charge and the charge collected by the electrodes is defined as the charge collection efficiency (CCE):

$$CCE = \frac{Q_{coll}}{Q_{gen}} \tag{6.4}$$

Combining Eq. 6.2 and Eq. 6.4, d_c can then be written as:

$$d_c = d \times CCE \tag{6.5}$$

The CCE has a dependence on the applied bias voltage and it can be measured using the beta sources as described in Section 6.2.1.

6.1.6 I-V measurement

Diamond has a very large resistivity ($> 10^{12}\Omega\cdot$cm), therefore the dark current of diamond is very low. However, as the dark current depends both on the quality of the diamond (crystallographic defects) and on the metallization quality of the diamond surfaces, I-V measurement should be done for each individual diamond to characterise the quality of fabrication. I-V measurement is the measurement of the dark current through a diamond sample as a function of the applied bias voltage. This measurement is essential to define the operational bias voltage range, within which the dark current is below certain level (normally $<$ nA).

For the I-V measurement a Keithley 6517B Electrometer was used [117]. This device can provide up to $\pm$1000 V at 1 mA and it can measure DC current from 10 aA to 21 mA. For the I-V measurement, Force Voltage Measure Current (FVMI) method was used. By using this method, the ammeter LO is connected to V-source LO internally as shown in Fig. 6.4.

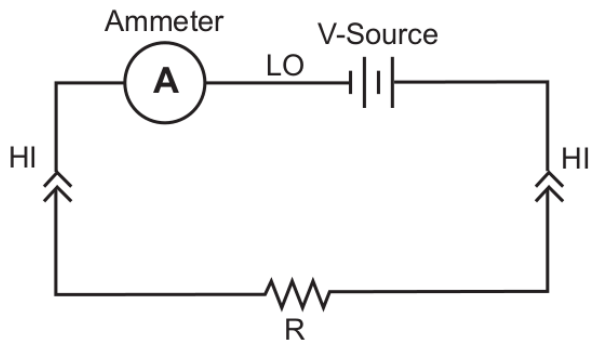

Figure 6.4: I-V measurement circuit using FVMI method, where R is replaced by DS in our measurements

LabWindows program was used for the control of the Keithley and for data taking. During the measurement, the bias voltage was changed with 10 V/step with a waiting time [1] of 60 s/step and the current was measured 10 times after the waiting time and averaged for each bias voltage. A measurement loop from -400V to 400V was set to measure the hysteresis behaviour of the I-V curve.

[1] After applying a bias voltage, it requires some time for the current to get settled. This settling process is studied in more detail in Ref. [116] and also discussed in Section 7.2.1.

DS samples

For the I-V measurement, we tested two samples of diamond. Sample No.1 is a sCVD diamond pad with a dimension of 4.6×4.6×0.5 mm and metallised with Ohmic DLC [1]/Pt/Au (4/20/200 nm) as electrodes on two surfaces (see Fig. 6.5 top left). This diamond pad was packaged in a dual ended isolated aluminium detector package with 2 SMA female connectors. The diamond is glued on the electrode from one side (for bias voltage), and connected via bonding wires from the other side (for signal readout), each side is connected to an SMA connector. The Al package serves also as a shielding for RF electromagnetic waves. On the top of the package there is a 1mm thick Al window with 2 mm aperture.

Sample No.2 is a "B1-HV sCVD Beam Loss Detector" fabricated by the CIVIDEC company (see Fig. 6.5 top right) [118]. This sample uses also a sCVD diamond pad with a dimension of 4.5×4.5×0.5 mm and metallised with gold as electrodes. It has a high-voltage input for the supply of the bias voltage and the signal is read out from the low-voltage side. The detector uses two PCBs to clamp the diamond in the middle and forms a 'sandwich'-like compact design with the two PCBs serving both for the electrical contact and for the RF shielding. Besides, an aluminium box can be used to cover the diamond with extra RF shielding.

Different from sample No.1, sample No.2 has a low-pass filter for the high-voltage supply and charging capacitors are implemented in order to compensate for the detector discharge. The charging capacitors have a capacity of 100 nF. The electronic circuit for sample No.2 is also shown in Fig. 6.5.

Measurement results

An example of the measured I-V curve for sample No.1 and No.2 is shown in Fig. 6.6 for a bias voltage from -400 V to 400 V. A clear hysteresis behaviour can be observed. The measured dark current level is higher for sample No.2 than for sample No.1. This might due to the electronic circuit on the sample No.2. For both samples, the measured dark current is a little bit higher for the positive bias voltage than for the negative bias voltage. The maximum dark current is at 100 pA level, which is quite low comparing

[1] Diamond-Like-Carbon (DLC) layer.

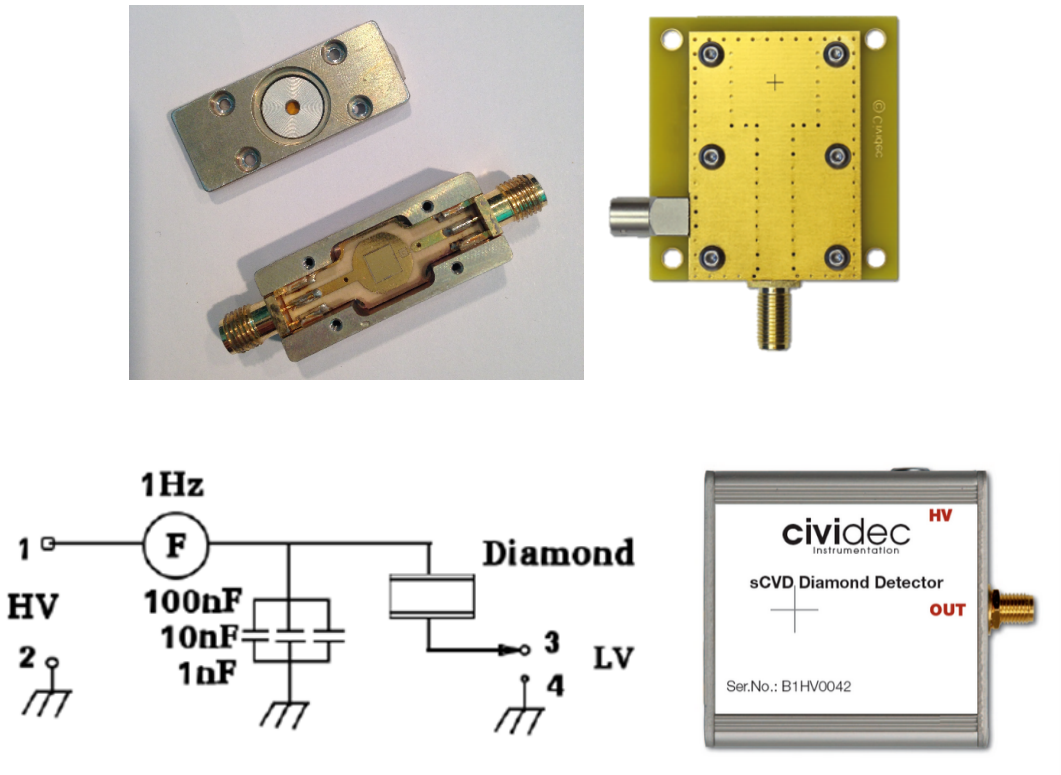

Figure 6.5: DS sample No.1 (upper left) and sample No.2 (upper right) with the electronic circuit (lower left) and the Al box (lower right)

with the expected signal level ($\sim \mu A$). Therefore, it can be concluded that the operational range from -400 V to 400 V is safe and with a very low dark current, which can be neglected.

6.1.7 Capacitance of CVD diamond

If we consider the diamond sensor as a parallel-plate capacitor constructed of two parallel plates, then the capacitance of a diamond sample can be calculated as:

$$C = \epsilon\epsilon_0 \frac{S}{d} \approx 2pF \tag{6.6}$$

where the permittivity of dielectric constant constant of diamond ϵ_0=5.7 and vacuum permittivity ϵ= 8.85×10^{-12} F/m, the diamond surface area S=4.5×4.5mm^2 and the diamond thickness d=500 μm. Therefore, for our sample a capacitance of 2 pF is expected.

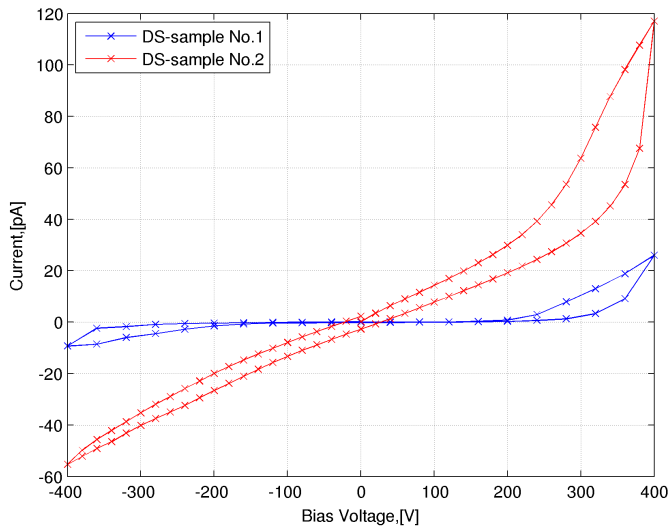

Figure 6.6: I-V measurement results for DS sample No.1 and sample No.2

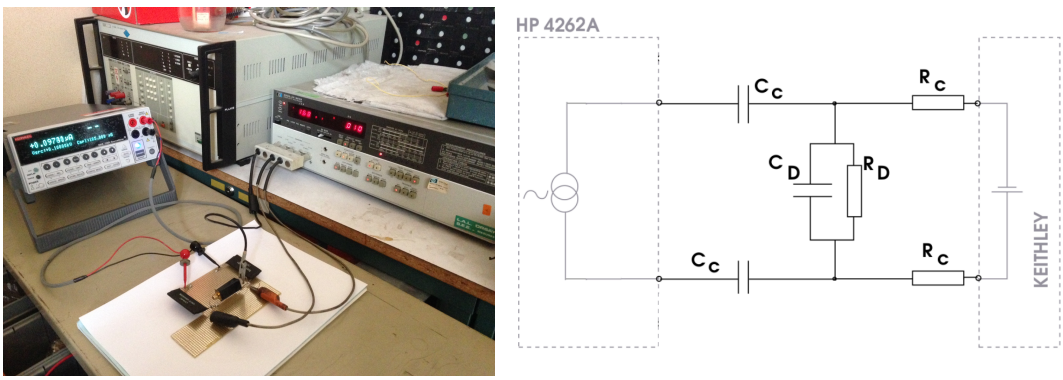

Figure 6.7: Capacitance measurement for DS sample No.1

For the measurement of the real capacitance of the diamond, which depends both on the quality of the diamond and on the metallization quality, a HP 4262A LCR meter was used. The LCR meter has a Wheatstone bridge inside and it can be used for the impedance measurement. The measurement circuit is displayed in Fig. 6.7. The LCR meter feeds an alternating current i = i_a sin(ωt) with ω=10kHz to the diamond sample via a PCB on which two large capacitors C_C=50 nF and two large resistors R_C=600 MΩ are mounted. A Keithley 2410 source-meter allows to apply a DC voltage to the sample. The bias voltage was raised up to 200 V with 10 V/step, the capacitance was measured at each step. The resistors $R_C \gg (\omega C_D)$ decouple the influence of the voltage

supply from the measurement circuit. The capacitors $C_C \gg C_D$ decouple the direct current component from the LCR meter [116].

Taking into account that $R_D \gg \frac{1}{\omega C_D}$ and $C_C \gg C_D$, the diamond impedance can be calculated as:

$$Z_D = \frac{R_D \cdot \frac{1}{\omega C_D}}{R_D + \frac{1}{\omega C_D}} \approx \frac{1}{\omega C_D} \tag{6.7}$$

The total measured total impedance then can be given as:

$$Z = \frac{1}{\omega C_C} + \frac{1}{\omega C_C} + Z_D \approx \frac{1}{\omega C_D} \tag{6.8}$$

from where the capacitance of diamond can be obtained.

The measured diamond capacitance is 1.68±0.01 pF for all the voltages. Therefore, no capacitance-voltage dependence was observed for this sample, and the measured capacitance is quite close to the expected value.

6.2 sCVD diamond characterisation using radioactive sources

Tests with radioactive sources were performed in a specially equipped clean room at LAL before testing the diamond detector at PHIL with large intensity electron beam. These tests are the standard tests to characterize each individual diamond detector. The measurements using β sources permit us to study the Landau distribution of MIPs and measure the CCE, and the measurements using α sources can be used for the the study of mobility, saturation velocity and lifetime of electrons and holes separately.

6.2.1 Measurements using β source

Electrons with energy more than 1.6 MeV are considered as MIPs for diamond [116]. For the characterisation of CVD diamond, Strontium-90(^{90}Sr) sources are usually used. ^{90}Sr undergoes β^- decay into Yttrium-90 (^{90}Y) with a maximum decay energy of 0.55 MeV, and its half-life time is 28.8 years.^{90}Y undergoes β^- decay to Zirconium-90(^{90}Z) with a half-life of 64 hours and a maximum decay energy of 2.28 MeV. The activity of the ^{90}Sr source used for our the measurement is 37 MBq.

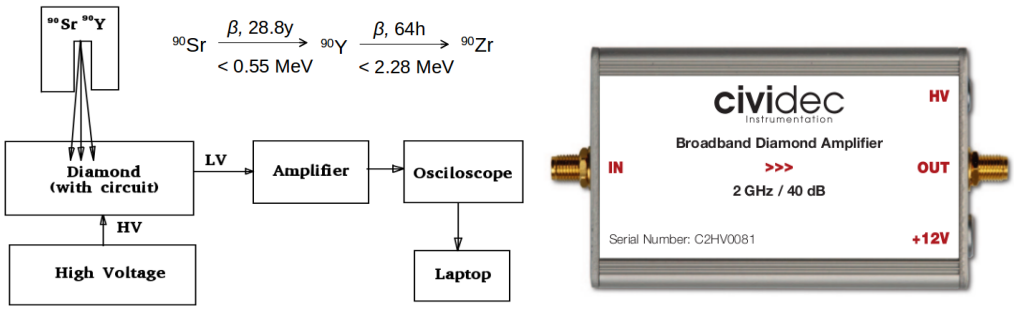

Figure 6.8: Left:Measurement set-up for test with radioactive sources and circuit diagram of diamond detector; Right: 40dB current amplifier used for the measurement.

Measurements using current amplifier

Fig. 6.8 shows the experimental set-up for the test with ^{90}Sr source and the 40 dB current amplifier (C2) used for the tests. The ^{90}Sr source was put on the top of the DS, and the DS was connected to the C2 amplifier via a SMA connector and then to the Agilent oscilloscope via a 1m RG58 coaxial cable. The C2 amplifier has a bandwidth of 2 GHz and a RMS output noise of 2.5 mV (3.5 dB).

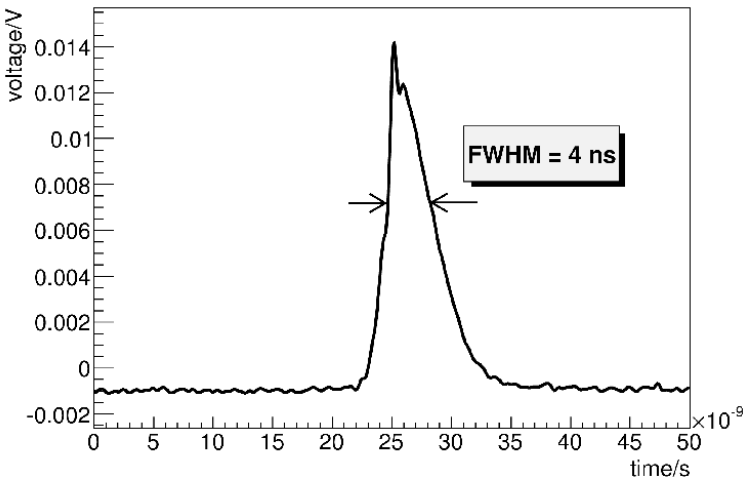

Figure 6.9: Averaged pulse of signal obtained from ^{90}Sr source with C2 amplifier (40 dB)

The pulse shape of the signal from ^{90}Sr source is shown in Fig. 6.9. The signal pulse shown is from averaging 1000 events. As the electrons and holes are generated all along the track of the MIPs, they start to be absorbed by the corresponding electrodes right

after their generation, therefore, the pulse has a triangular shape [102]. The FWHM of the pulse is around 4 ns. The pulse was obtained in self-trigger mode with 5 mV trigger level. The noise RMS and signal amplitude for the 1000 events is shown in Fig. 6.10 (a). The noise level obtained from the measurements is 2.0±0.2 mV and the signal amplitude is 16.0±2.8 mV (before normalisation by 40 dB).

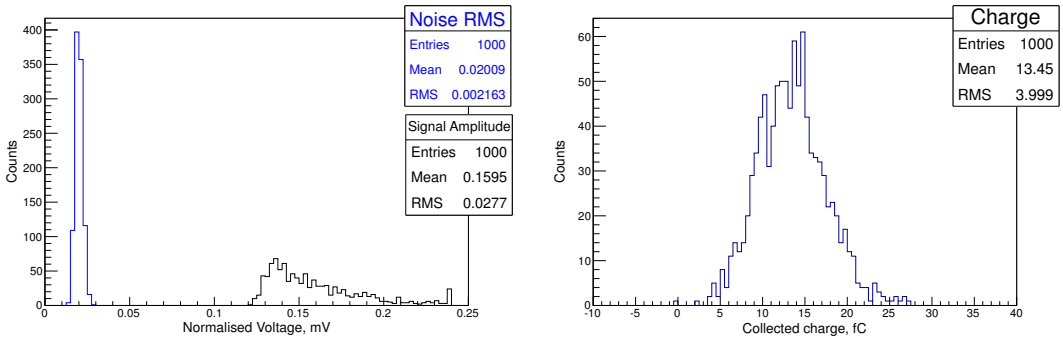

(a) **(b)**

Figure 6.10: Signal and noise amplitude distribution (a) and signal charge distribution (b) measured using current amplifier with self-trigger.

As the signal was obtained with 5 mV of self-trigger level, the lower energy electrons (< 1.6 MeV) are not eliminated in the system. Therefore, we collected a mean charge of 13.45 fC instead of 2.88 fC as expected for 1 MIP as shown in Fig. 6.10 (b). As the expected signal amplitude for 1 MIP is around 3.6 mV (with 40 dB amplifier), it is difficult to detect 1 MIP with the C2 amplifier in self-trigger mode. Therefore, a new system with a charge amplifier and a scintillator as external trigger were prepared for the detection of MIPs.

Measurements using charge amplifier

The measurement set-up is shown in Fig. 6.11 together with the amplifier used the measurements. The amplifier (C6) used is a fast charge amplifier with a rise time of 3.5 ns and a Gaussian pulse shape with a FWHM of 10 ns. It is optimized for high-speed single MIP particle detection. The equivalent noise charge (ENC) is 1000 electrons comparing to 10000 electrons for C2 current amplifier. The gain of the amplifier is 4 mV/fC and the signal to noise ratio (SNR) is 6/fC.

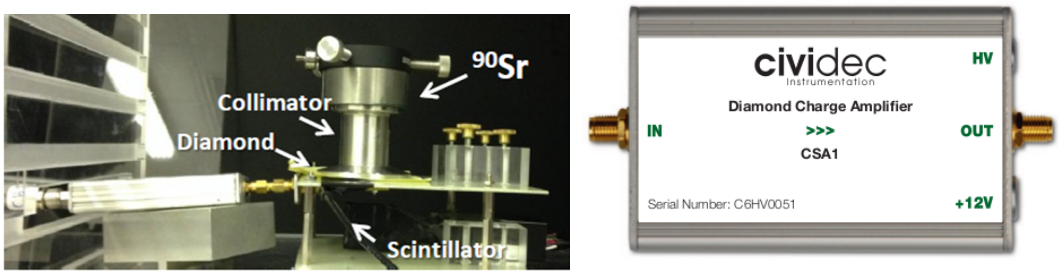

Figure 6.11: Measurement setu-up for the detection of MIPs using an external trigger from a scintillator

A 4 cm long aluminium collimator with diameter of 4 mm was used to collimate the emitted electrons. Under the collimator there is the DS and the scintillator. The distance between DS and sintillator is around 1.5 cm. The surface of the scintillator is $3{\times}3cm^2$, which is relatively large compared to the DS. Therefore, we expect that in addition to the electrons which pass through both the DS and the scintillator, there are electrons which pass through the edge of the collimator and reach the scintillator without passing through the DS. These electrons can generate a signal on the scintillator and set a trigger for DS, but they don't deposit energy in the DS.

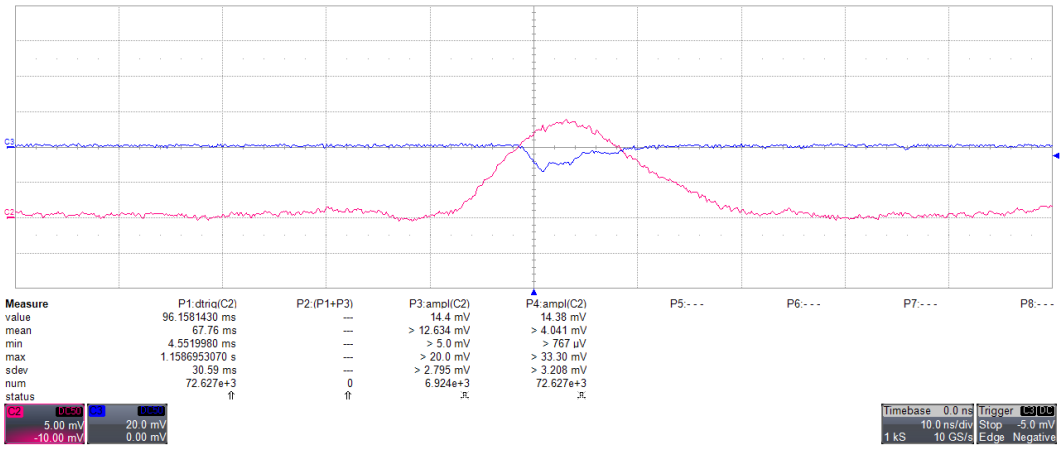

Figure 6.12: Signal waveforms of scintillator (blue) and DS (red) with trigger on scintillator

During the experiment, around 10^5 events were taken. The waveforms on the scintillator and the DS are shown in Fig. 6.12. The noise RMS was calculated for each waveform by taking the RMS of the first 400 points (before the signal start). Fig. 6.13 shows

the histogram of the noise RMS and the amplitude of waveforms. From the upper plot in Fig. 6.13, it can be seen that the measured noise level is 0.515±0.167 mV, which is quite consistent with the expected noise level: $1000e^{-}\times 1.6\times 10^{-19}\times 4mV/fC = 0.64mV$.

However, for the signal amplitude, besides the Landau distribution, which starts from 10mV, we observed more events triggered on the electrons which didn't go through the DS. In order to get the Landau distribution, the events with amplitude below 10 mV were eliminated from the data, and the rest of the events was fitted to a Landau distribution as shown in the lower histogram in Fig. 6.13. For the fit a Most Probable Value (MPV)[1] of 11.48 mV was obtained. This indicates an integrated charge of 2.87 fC, which confirms the former calculated expected value of 2.88 fC for MIPs.

6.2.2 Measurements using α source

As estimated penetration depth of α particles is less than 20 μm in diamond which is small compared to the 500 μm thickness DS, the electron hole pairs generated in this process can be considered as a thin layer of charge. Therefore, the measurements using α sources is considered as one of the transient current techniques (TCT) for detector characterization.

For the α particles injection, an ^{241}Am source with an activity of 3.9 kBq was mounted with a distance of 2 mm on the top center of the diamond, where a 1 mm diameter hole was specially made on the PCB for this test. The energy of the alpha particles emitted from ^{241}Am source is around 5.4 MeV.

When a bias voltage is applied to the DS, the width of the signal collected by the electrode close to the source is only in the order of several ps (around 6 ps for 400 V of bias voltage supposing a drift mobility of 2000 cm^2/V/s), thus it can not be seen on the scope with a sampling speed of 10 Gs/s. Therefore, the signal displayed on the scope is generated only by the charge (either electrons or holes) collected on the other electrode. By changing the polarity of the bias voltage, we can study signal from the electrons and holes separately.

Fig. 6.14 shows pulse shapes from electrons and holes by averaging 1000 events for data taken at different bias voltages. A Matlab [119] program was written to control the power supply and the scope simultaneously. The bias voltage was changed from -100 V to 400 V with a step of 50 V. The settling time between each step is 600 s. A self-trigger

[1] Peak of the Landau distribution

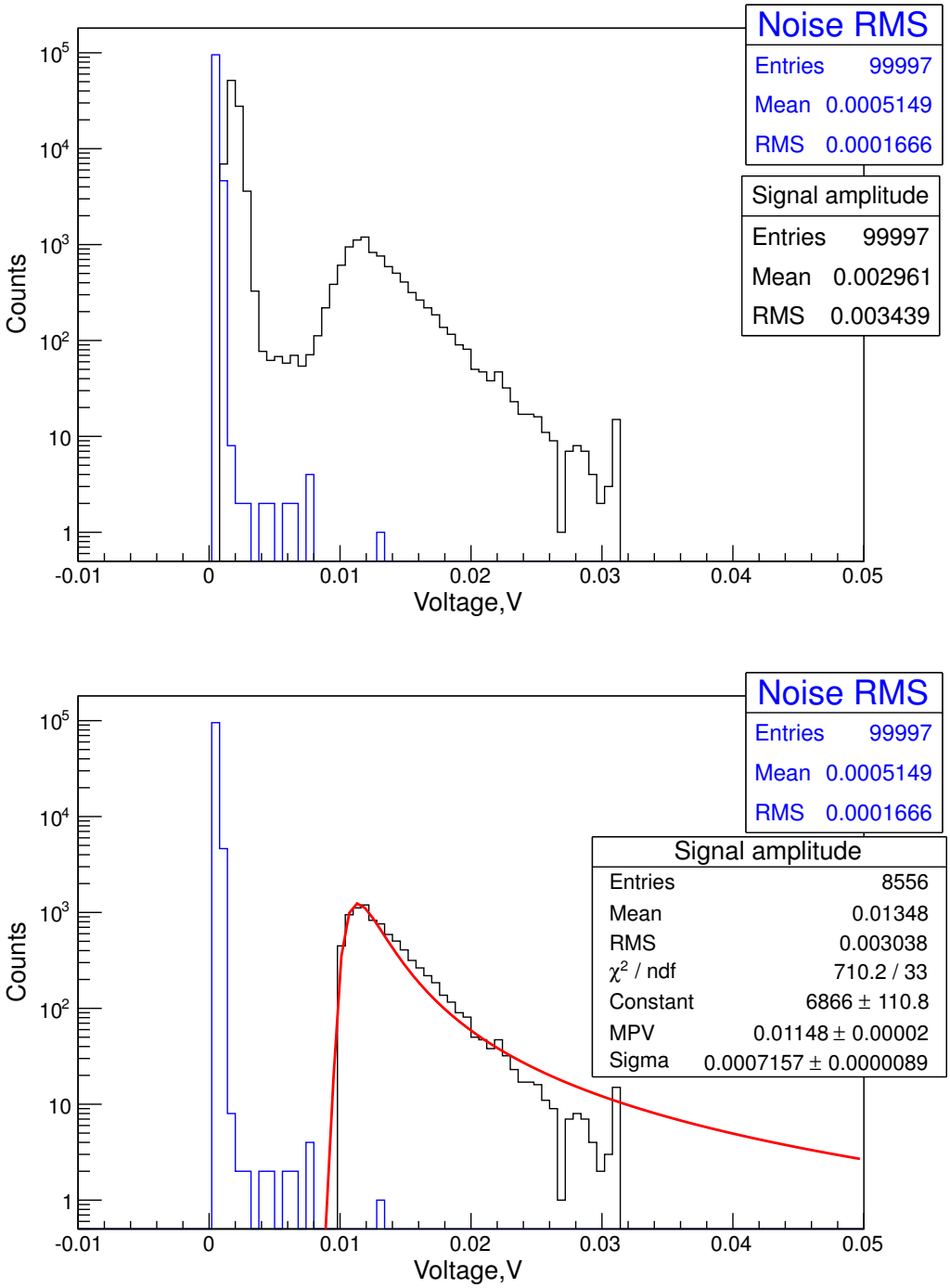

Figure 6.13: Signal and noise distribution measured using charge amplifier with external trigger given by the scintillator for all the recorded events (upper) and events above 10 mV fitted to Landau distribution (lower)

level of ±10 mV was applied for positive and negative bias voltage separately. The 40 dB C2 current amplifier was used for the measurements. For the measurements with lower than -100 V for electrons and lower than 100 V for holes, the ±10 mV trigger level is too high, as the trigger level is limited by the noise level of the C2 amplifier, we couldn't lower down the trigger level.

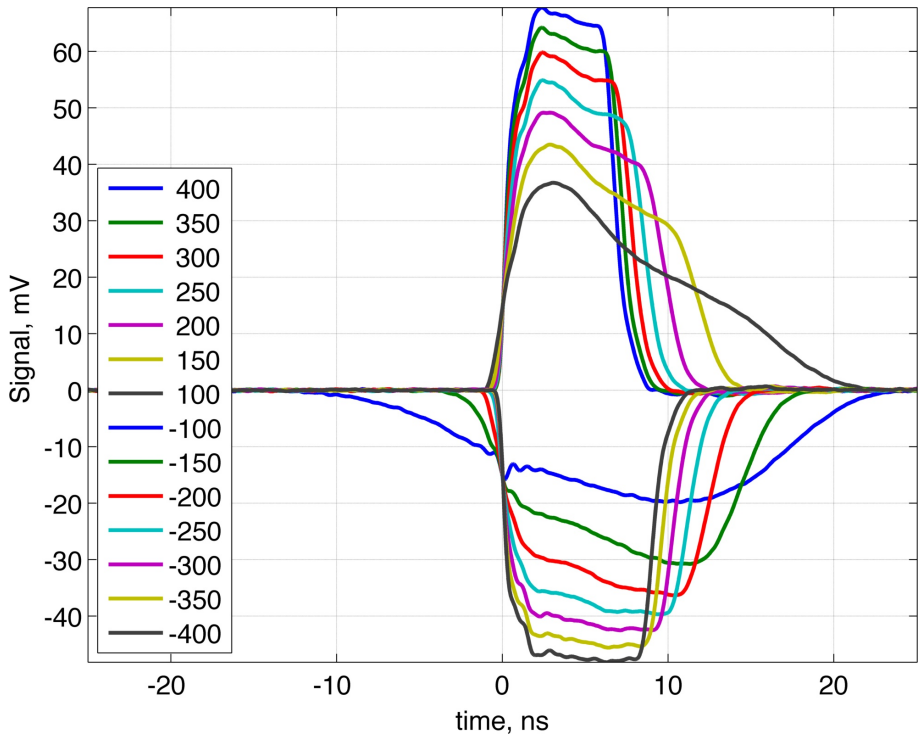

Figure 6.14: Signal from collected electrons (negative pulse) and holes (positive pulse)

From Fig. 6.14 it can be seen that pulse width increases as the bias voltage decrease. The rise time of the current signal is dominated by the time constant of the electronic circuit. With around 2 pF of capacitance for the DS, the rise time is around 0.1 ns. After this fast rising, the signal level should keep constant during the drift of charge-carriers. However, as there is a net effective space charge in the diamond bulk, we observe an increasing current for electrons and a decreasing current for holes, which indicates a negative space charge in the bulk. This space charge effect is explained in more detail in Ref. [120].

In the 1000 events taken at each voltage, there are small part of "bad" events which maybe caused by the RF pick-up in the outside environment. Therefore, a signal

selection criteria with collected charge $Q_{coll} > 20fC$ and $t_{FWHM} > 6ns$ was set for all the events. Fig. 6.15 shows the distribution of Q_{coll} for the selected events at 400 V and Q_{coll} as a function of applied bias voltage. The collected charge get saturated by applying higher than ∼150 V for the holes and the electrons collections. The maximum collected charge at 400 V is 67.7±1.9 fC for holes and 66.6±5.0 fC for electrons. As the mean ionization energy is around 13 eV in diamond, the expected charge from the α source is around 66.5 fC. Therefore, the CCE of this diamond sample is 100% for both electrons and holes at 400 V.

6.3 Lifetime of the charge-carriers

The lifetime of the charge-carriers($\tau_{e,h}$) is defined as the time for the total generated charge Q_0 to decrease by factor e^{-1}. It can be derived from the measurement using α sources. Besides, the charge-carrier mobility and saturation velocity can also be determined using this TCT method.

The instantaneous current (*i(t)*) induced by the charge-carrier movement in an intrinsic DS can be described using the simplified relation as shown in Eq. 6.9 [121]:

$$i(t) = \frac{Q_0 \cdot \mu_{e,h} \cdot E_0}{d} e^{\frac{t}{\tau_{eff_{e,h}}} - \frac{t}{\tau_{e,h}}} \tag{6.9}$$

where Q_0 is the total induced charge, $\mu_{e,h}$ the mobility of electrons and holes, E_0 the electric filed, d the thickness of DS, $\tau_{e,h}$ the lifetime of electrons and holes, and $\tau_{eff_{e,h}}$ the space charge effect time constant.

The mobility of electrons and holes in Eq. 6.9 can be calculated as:

$$\mu_{e,h} = v_{dr}\frac{d}{V} \quad with \quad v_{dr} = \frac{d}{t_{tr}} \tag{6.10}$$

where v_{dr} is the drift velocity, V the bias voltage, d the thickness of diamond and t_{tr} the transit time of charge.

The space charge effect time constant in Eq. 6.9 is defined as:

$$\tau_{eff_{e,h}} = \frac{\epsilon\epsilon_0}{e_0 \cdot \mu_{e,h} \cdot N_{eff}} \approx \frac{\epsilon\epsilon_0 t_{tr} V}{e_0 \cdot d^2 \cdot |N_{eff}|} \tag{6.11}$$

where ϵ_0 and ϵ are the permittivity of dielectric constant constant of diamond and vacuum permittivity, e_0 the electron charge, N_{eff} the net effective fixed space charge in the diamond bulk.

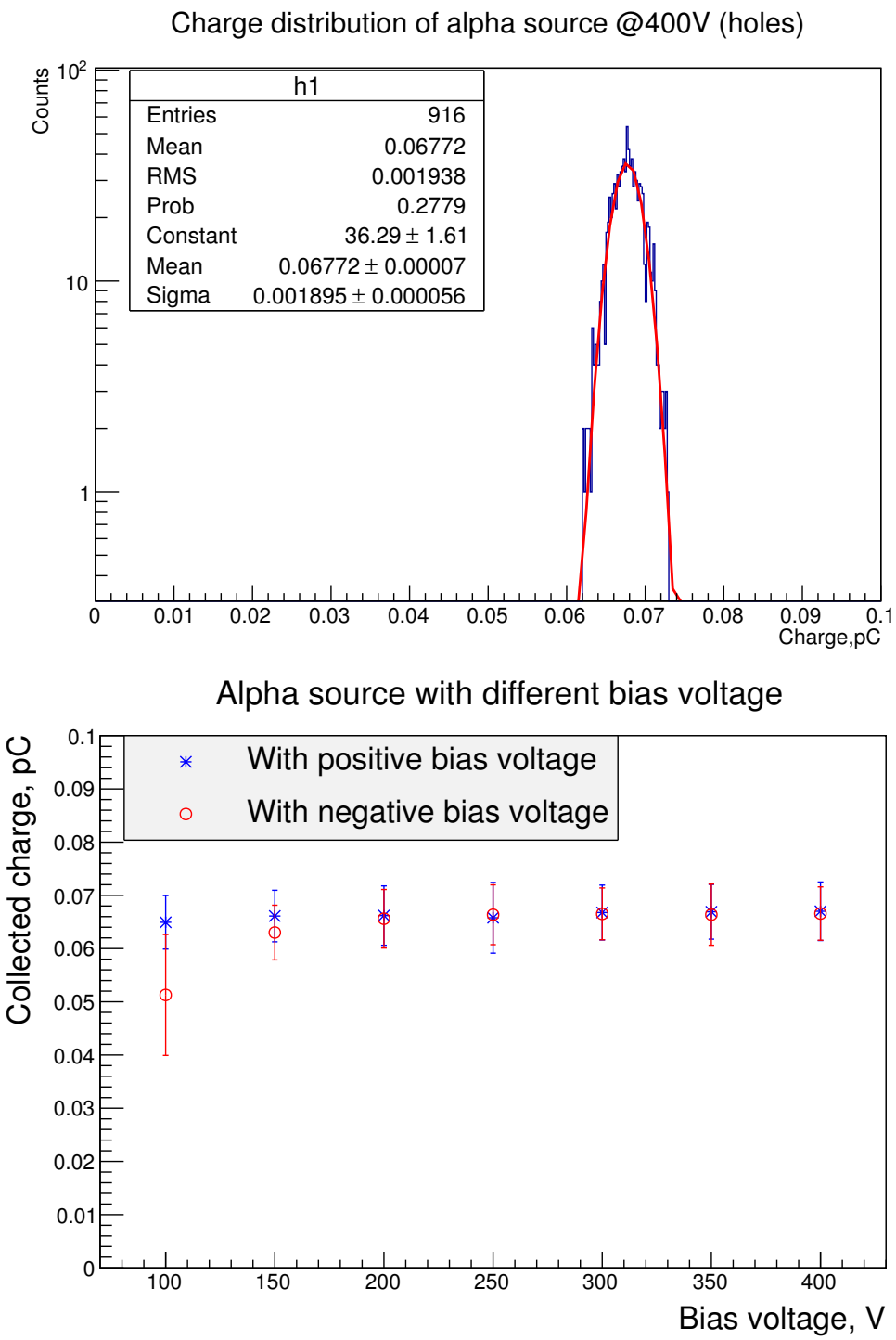

Figure 6.15: (a): Histogram of charge collected from the alpha source; (b):Collected charge as a function of bias voltage for electrons (red) and holes (blue)

The drift velocity of the charge-carriers in the diamond as a function of electric field E can be described using the empirical formula [120, 122]:

$$v_{dr} = \frac{\mu_{0_{e,h}} \cdot E}{1 + \frac{\mu_{0_{e,h}}}{v_{sat_{e,h}}} \cdot E} \tag{6.12}$$

where $\mu_{0_{e,h}}$ is the low-field mobility for electrons and holes and $v_{sat_{e,h}}$ the saturation velocities for electrons and holes.

In the measurements, the drift velocity can be defined as $v_{dr}(E) = d/t_{tr}$ as shown in Eq. 6.10. The transit time (t_{tr}) was taken as the FWHM of the signals in Ref. [121] and taken as the total transit time t_{tr}=t_e-t_s in Ref. [120]. In our data analysis, we took the FWHM of the signals.

Fig. 6.16 shows the drift velocity as a function of applied electric field. The curves for electrons and holes were fitted according to Eq. 6.12. From the fit parameters of the curves, the mobility and saturation velocity of electrons and holes can be obtained.

The total induced charge can be defined as the integration of the measured current pulse:

$$Q_{e,h}(V) = \int_0^{t_{tr}} i_{m_{e,h}}(V,t)\,\mathrm{d}t \tag{6.13}$$

by inserting Eq. 6.9 into Eq. 6.13 and assuming $\tau_{e,h} \gg t_{tr}$, we can get a solution as:

$$Q_{e,h}(V) = Q_{0_{e,h}} \left(\frac{\tau_{e,h}}{t_{tr}}\right) \left(1 - e^{-\frac{t_{tr}}{\tau_{e,h}}}\right) \approx Q_{0_{e,h}}(1 - \frac{t_{tr}}{2\tau_{e,h}}) \tag{6.14}$$

as t_{tr} can be expressed by the inverse drift velocity as d/v_{dr}, the measured charge $Q_{e,h}(V)$ can be plotted as a function of inverse drift velocity $1/v_{dr}$ as shown in the bottom plot in Fig. 6.16. The data were fitted linearly to extrapolate the lifetime using Eq. 6.14.

The extrapolated values of low-filed mobility (μ_0), saturation velocity (v_{sat}), lifetime (τ) and the calculated maximum charge collection distance ($d_{c_{max}} = v_{sat} \times \tau$) of electrons and holes are shown in Table 6.2. It can be seen that the $d_{c_{max}} \gg 500\mu$m, the thickness of DS.

6.4 Tests of in air diamond sensor at PHIL

After the characterization of the diamond samples in the clean room, tests with electron beam are needed to see the waveform shapes for different beam intensity, measure the

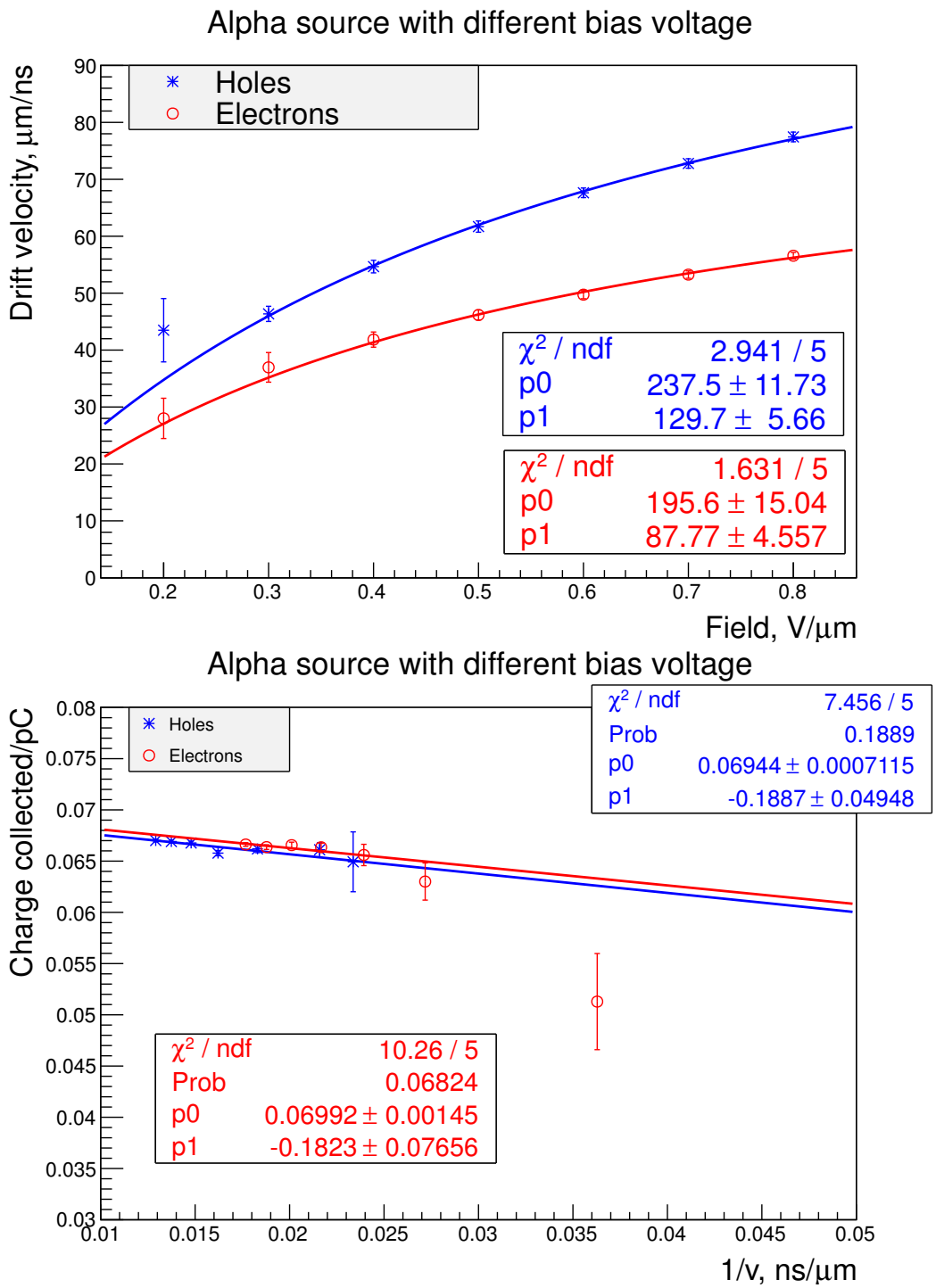

Figure 6.16: Upper: drift velocity as a function of electric field; Lower: Collected charge as a function of inverse drift velocity

	μ_0, $[cm^2/\mathbf{Vs}]$	v_{sat}, $[\mu\mathbf{m/ns}]$	τ, [ns]	d_{cmax}, [mm]
electrons	1956± 150.4	87.77± 4.56	92.00±25.07	8.07±2.24
holes	2375± 117.3	129.7± 5.66	95.89±42.24	12.44±5.50

Table 6.2: Charge transport parameters of DS sample No.2

linearity response of the diamond and to test the fast remote readout system. The first tests were done for sample No.1 starting in June 2013, and the tests for sample No.2 were started in Oct. 2013. In this section most of the results presented were obtained from the tests done with sample No.2.

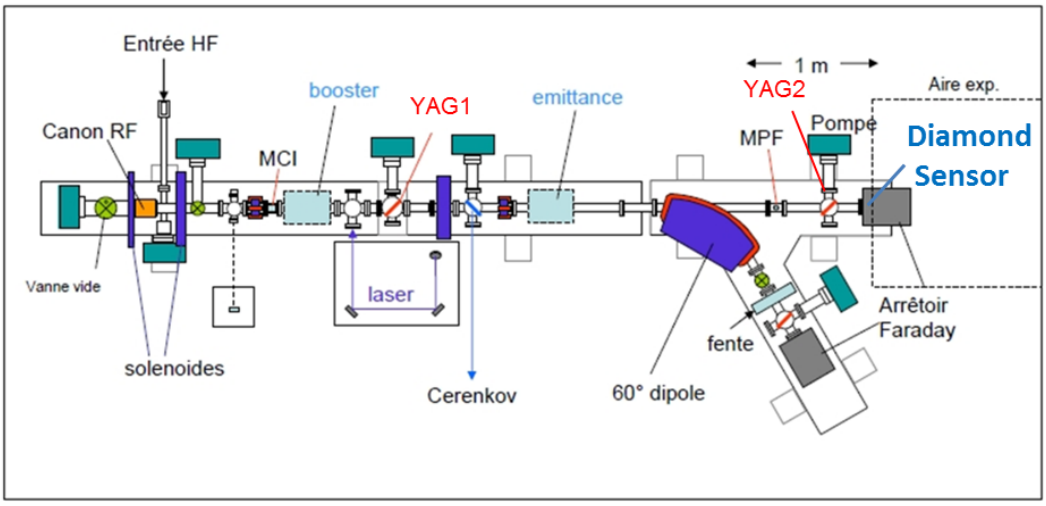

Figure 6.17: Layout of PHIL

The tests with electron beam were done at PHIL (see Fig. 6.17). PHIL is a 5 m long photoinjector beamline at LAL, which provide a short pulse (7 ps) electron beam with low emittance ($10\pi \cdot mm \cdot mrad$) and low energy from 3 MeV to 5 MeV [123]. The electrons with this energy are well considered as MIPs. The bunch frequency at PHIL is 5 Hz. The electron beam charge can be varied from less than 1 pC to 2.2 nC at the exit window by changing the laser density shining on the Mg cathode. The laser density can be adjusted either by adding filter cards with discrete values (eg. 3%, 50%, 70%) or by rotating a filter window with continuous values. However, as the dependence of the ejected electron beam intensity on the laser density is not linear, the charge of the electron beam should be measured each time after changing the laser density.

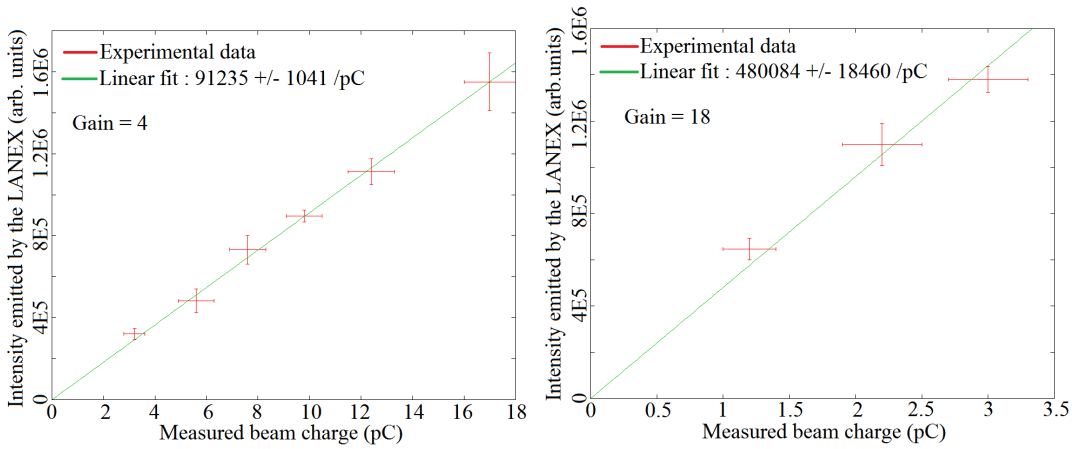

Figure 6.18: Calibration for LANEX screen [57].

The charge of the electron beam can be measured by the two Integrating Current Transformers (ICT1 and ICT2) installed along the beam line. ICT1 is about 1 m from the cathode and ICT2 is just before the 18μm thick Ti exit window, at the end of the 5 m straight line. After the exit window, the charge can be measured by another removable ICT (ICT3) or by a Faraday cup, the measurement ranges of which are from 1 pC to 2 nC. For the charge measurement below 1 pC, a 100 μm thick YAG:Ce screen with a CCD camera can be used, this can bring the lower charge measurement limit to 0.5 pC. For lower than 1 pC measurement, we used a LANEX (R) screen, which has higher light yield and less blurring effects. The light emitted from the Lanex screen was calibrated with the charge measured by Faraday cup (see Fig. 6.18). The calibration was done for different factor of gain to enable measurement with large dynamic range. Extrapolating that calibration below the sensitivity of the Faraday cup enabled the LANEX screen to be used for beam charges as small as 33±11 fC [57].

The beam size at PHIL can be measured by the two YAG:Ce screens (YAG1 and YAG2) in the beamline and by the YAG:Ce screen (YAG3) or the LANEX screen installed after the exit window. The typical beam size is around 2 mm×2 mm at the exit window.

6.4.1 Experimental set-ups

Fig. 6.19 shows the experimental setup for diamond detector test at PHIL. A 4 cm long Al collimator with 2 mm diameter was used to collimate the beam after the exit window.

The diamond detector was mounted next to the LANEX screen on a transverse movable stage after the collimator. The output signal was connected with a 100 m (50 m of 1/2 inch plus 50 m of 1/4 inch) long high quality LDF1-50 HELIAX RF low density foam coaxial cable to the control room, where we used an Agilent 6104 oscilloscope with 4 Gs/sec sampling rate and 1 GHz bandwidth to read the signal pulse. A 50 Ω feed through terminator was used to enable the 1 MΩ coupling on the scope, and the signals were viewed with the 50 Ω termination by the scope. The scope was controlled remotely using Labview installed on the laptop.

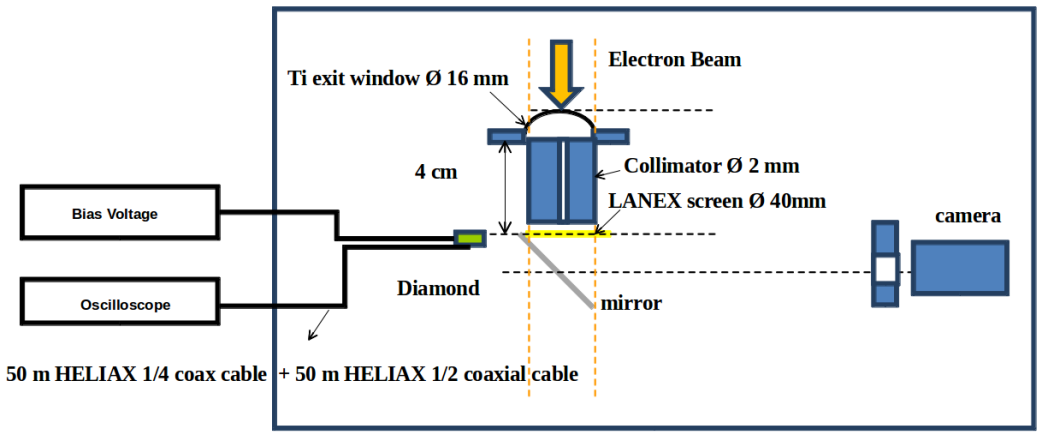

Figure 6.19: Experimental setup at PHIL.

Coaxial cables and signal attenuation

Since 100 m long coaxial cables are used for the fast signal transmission at PHIL, it is essential to study different types of coaxial cables and to avoid the signal attenuation and distortion by using high quality coaxial cables.

The coaxial cable conducts electrical signal using an inner conductor (usually a solid copper, stranded copper or copper plated steel wire) surrounded by an dielectric layer and all enclosed by a shield, typically braided flexible shield or solid tube semi-rigid shield. Outside of the shield the cable is protected by an outer insulating jacket (see Fig. 6.20).

Signal attenuation (loss) on the coaxial cable depends on the loss in the dielectric material filling the cable, and resistive losses in the center conductor and outer shield. These losses are frequency dependent, the losses becoming higher as the frequency

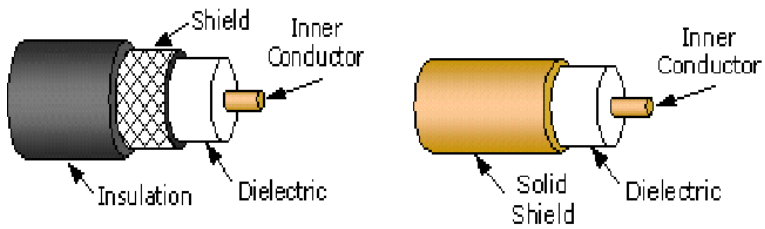

Figure 6.20: Structure of coaxial cables with braided flexible shield (left) and solid tube semi-rigid shield (right)

increases [124]. The loss per meter of cable can be calculated according to the following equations:

$$\alpha_{conductors} = \frac{11.39}{Z} * \sqrt{f} * (\frac{\sqrt{\rho_{rd}}}{d} + \frac{\sqrt{\rho_{rD}}}{D}) \tag{6.15}$$

$$\alpha_{dielectric} = 90.96 * f * \sqrt{\varepsilon_r} * tan(\delta) \tag{6.16}$$

where:

- $\alpha_{conductors}$ = losses in the conductor in dB/m
- $\alpha_{dielectric}$= losses in the dielectric in dB/m
- d = outside diameter of inner conductor in mm
- D = inside diameter of outer conductor in mm
- ε_r= relative dielectric constant
- f = frequency in GHz
- ρ_{rd}= inner conductor material resistivity relative to copper
- ρ_{rD} = outer conductor material resistivity relative to copper
- δ = loss tangent

The loss on the inner conductor is also called Skin Effect losses. It is the dominating loss when the signal frequency is below 10 GHz as shown in Fig. 6.21. This loss can be reduced by increasing the inner conductor diameter of the cable. A cable with twice the diameter will have half the skin effect resistance. Ignoring dielectric and other losses, the larger cable would halve the dB/meter loss.

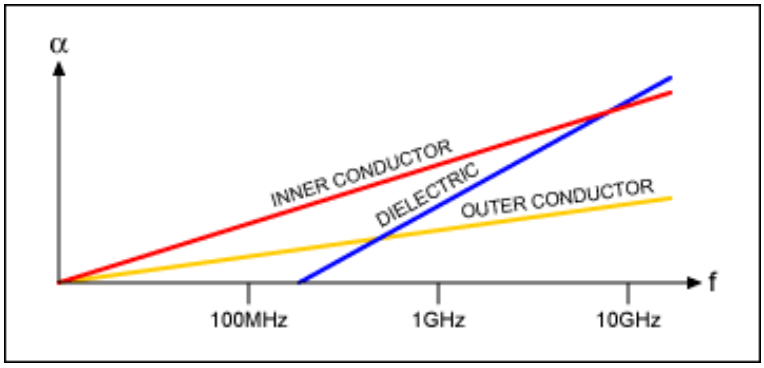

Figure 6.21: Representation of inner conductor (skin effect), dielectric, and outer conductor (return-path) losses as a function of frequency

Measurements of cables

In order to avoid signal attenuation and prevent the deformation of the pulse shape due to the cable, coaxial cables with 50 Ω impedance are used for the fast signal transmission.The cables were tested at LAL using a fast pulse generator (Picosecond step generator 4050B). An input square pulse with 10 ns width, ∼45 ps rise time and 5.22 V amplitude was generated and sent to the oscilloscope.The pulse shapes were compared for the signal transmission with and without the cables. Tests of all the types of cables with different lengths are summarised in Table 6.3.

	Length	Input Width	Output Width	t_{rise}	t_{fall}	Atten.
RG58	10m	2ns	2.163ns	1.073ns	1.487ns	1.16dB
	20m	2ns	2.256ns	1.202ns	2.457ns	2.50dB
	50m	2ns	2.783ns	1.358ns	4.211ns	9.63dB
1/4 inch	50m	10ns	10.25ns	0.703ns	0.75ns	0.44dB
1/2 inch	50m	10ns	10.1ns	0.733ns	0.5ns	0.37dB

Table 6.3: Cable test results

Two examples of the test results for 50 m RG58 and 1/4 inch Heliax cable are shown in Fig. 6.22. We can see that the attenuation and deformation of the pulse is much less for the 1/4 inch Heliax cable than for the RG58 cable. Thus for long distance (>10m) signal transmission, we have chosen the 1/4 inch and 1/2 inch Heliax cables. And we used RG58 cables only for short distance signal transmission in the tests.

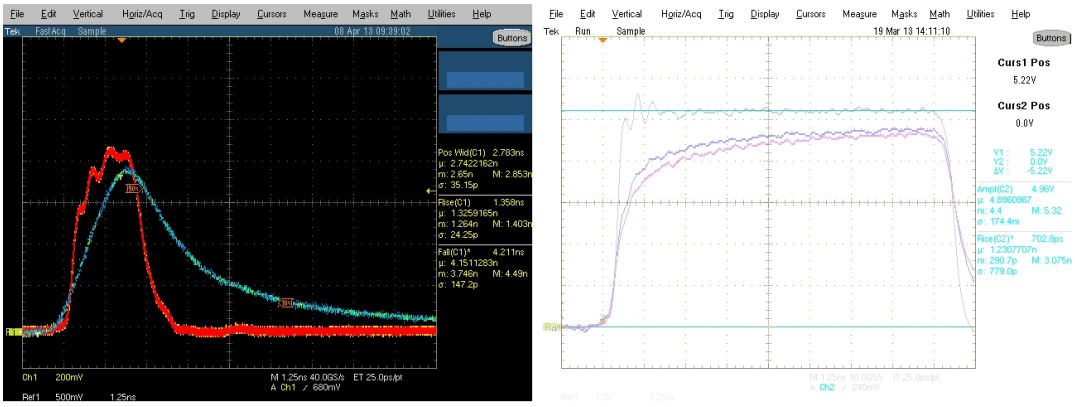

Figure 6.22: Left: Test of 50m RG58 cable with 2 ns input pulse (red) and output pulse after cable (blue); Right:Test of 1/4 inch Heliax coaxial cables with 10 ns input pulse w/o cable (gray) and output pulse after 1/4 inch cable (2 cables,50 m each) (pink and purple)

6.4.2 Experimental results

Pulse waveforms

In the tests using β source we have shown that the typical pulse width for a MIP particle is around 4 ns (see Fig. 6.9). However, at PHIL we have observed that with increasing number of incident electrons, the pulse width also increases. Fig. 6.23 shows an example of the pulse form for different beam intensity. The charge of the beam was measured by the LANEX screen. We can see that the pulse fall time increases with the beam intensity, while the rise time stays almost constant.

As mentioned in Section 6.2.1 the rise time of the current signal is dominated by the time constant of the electronic circuit. Therefore, it doesn't change with the input beam intensity. However, the fall time, which indicates the time for the charge carriers to arrive on the electrodes, highly depends on the charge carrier drift velocity. We have shown before that the drift velocity depends on the electric field as expressed by Equation 6.12, therefore, the increasing fall time indicates a decreasing electric field in the DS. This can be explained by the voltage drop on the 50 Ω readout resistor which is used for the impedance matching for the coaxial cable as shown in Fig. 6.3. The voltage drop (V_{drop}(t)) can be expressed as:

$$V_{drop}(t) = I(t) \times 50\Omega \tag{6.17}$$

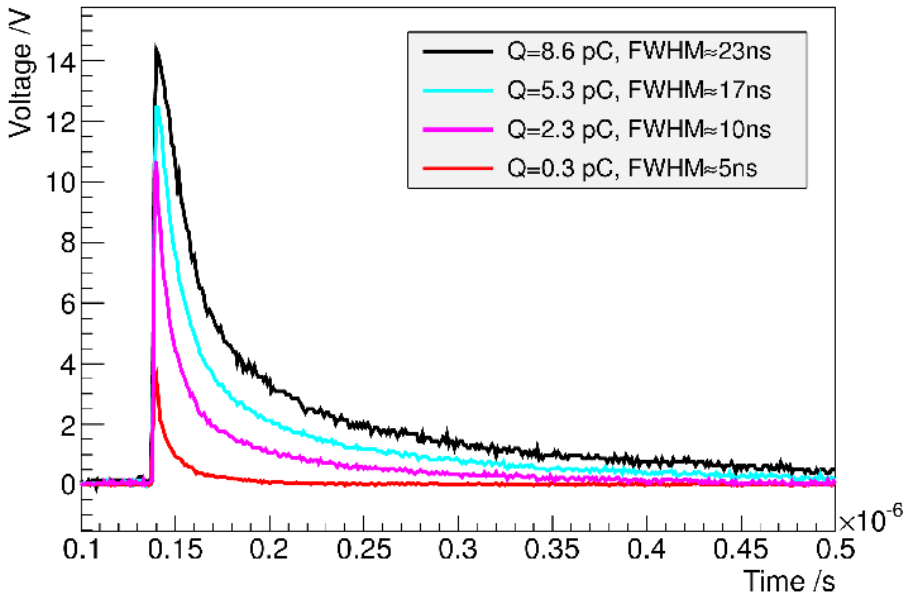

Figure 6.23: Signal pulse form for different injected beam intensity

therefore the effective bias voltage (V_{eff}(t) applied on the DS can be described as:

$$V_{eff}(t) = V_{bias} - V_{drop}(t) \tag{6.18}$$

where V_{bias} is the applied bias voltage.

In order to study the effect of voltage drop on the linearity response of signal amplitude and signal charge, measurements were done for a large range of incident beam intensity using the calibrated LANEX screen for the measurement of total charge.

Number of incident electrons

In the experiment, the LANEX screen is not only used for the total charge measurement, but also for the beam size measurement. As the beam core follows Gaussian distribution after the exit window, knowing the beam size, the number of electrons intercepted on the diamond can be calculated by the following formula:

$$N = \frac{N_t}{2 * \pi * \sigma_x * \sigma_y} \int_{-\frac{1}{2}l_x}^{\frac{1}{2}l_x} e^{-\frac{x^2}{2\sigma_x^2}} \, \mathrm{d}x \int_{-\frac{1}{2}l_y}^{\frac{1}{2}l_y} e^{-\frac{y^2}{2\sigma_y^2}} \, \mathrm{d}y \tag{6.19}$$

where N_t is the total number of electrons, σ_x and σ_y the measured horizontal and vertical beam size, l_x and l_y the horizontal and vertical width (4 mm).

Dependence of signal amplitude on intensity

The dependence of signal amplitude on intensity is shown in Fig. 6.24. During the measurement, 10 images were taken by the LANEX screen at each intensity to get the averaged charge and beam size for calculating the number of intercepted electrons. It can be seen that the fluctuation of the measurements is much more significant for lower intensity than for higher intensity.

The pulse amplitude starts to get saturated after an injection of more than 2×10^6 electrons (0.32 pC). The saturation of pulse amplitude can be explained by the voltage drop on the DS when a large current go through the 50 Ohm terminator, which means a reduction on the electric field and consequently on the drift velocity of the electrons and holes. This can also lead to electron-hole recombination if the collection time gets larger than the recombination time.

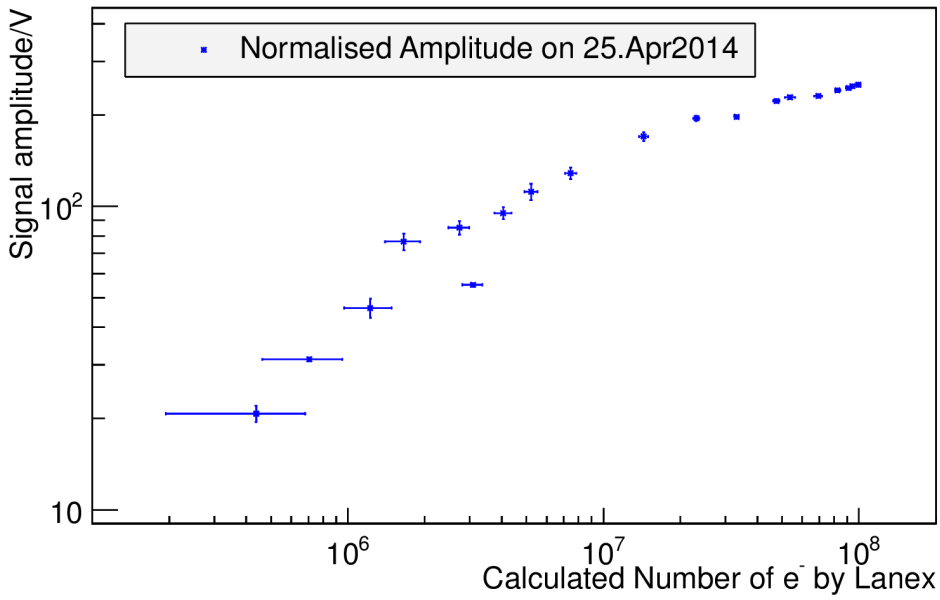

Figure 6.24: Signal amplitude as a function of number of input electrons.

Dependence of collected charge on intensity

When the recombination of electrons and holes happens inside the DS, then part of the charge disappears, consequently less charge is collected. This can result in the saturation of charge collection. A hint of such saturation in the collected charge (obtained

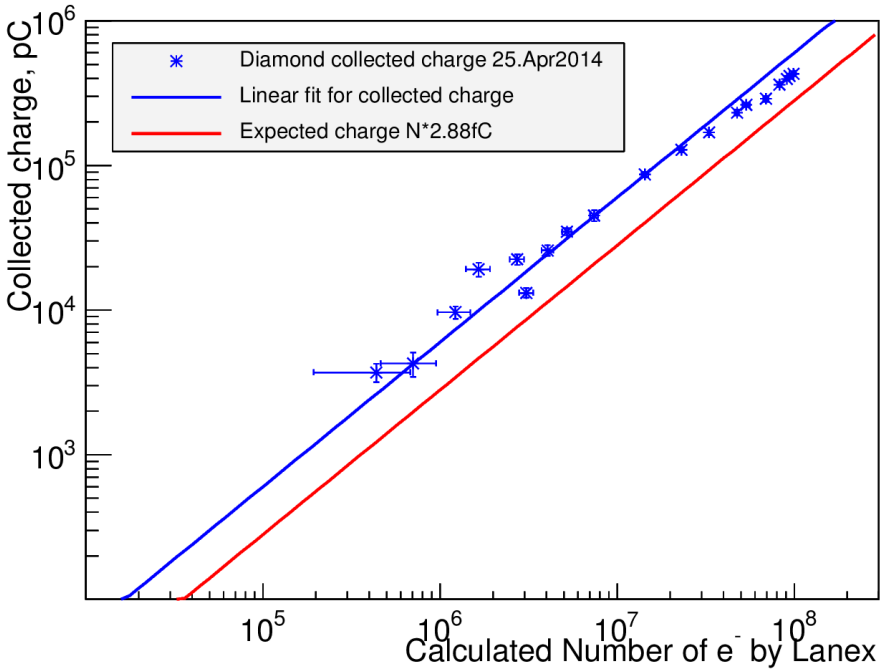

Figure 6.25: Collected charge as a function of number of input electrons.

by integrating the signal pulse above the pedestal) can actually be seen in Fig. 6.25 for input charges larger than 2×10^7 electrons (3.2 pC). Below such values, the response in terms of collected charge is linear. A factor 2 difference was observed with the expected signal as calculated multiplying the charge generated by 1 MIP (2.88 fC) by the number of electrons derived from the charge measurement using the LANEX. This may be due to the calibration of the LANEX.

Beam size measurement

Beam size measurement were performed using the two diamond samples with a movable stage installed after the exit window. The measured beam size can be extrapolated from the signal amplitude distribution as far as the signal amplitude is not saturated (<100 V as can be seen from Fig. 6.24).

Suppose the beam distribution after the exit window is Gaussian, then the measured distribution is a convolution of Gaussian distribution and uniform distribution given by the strip width. Similar to the beam size measurement using wire scanners, by changing the variance of circular distribution ($\frac{d}{4}^2$) to the variance of uniform distribution ($\frac{d}{12}^2$)

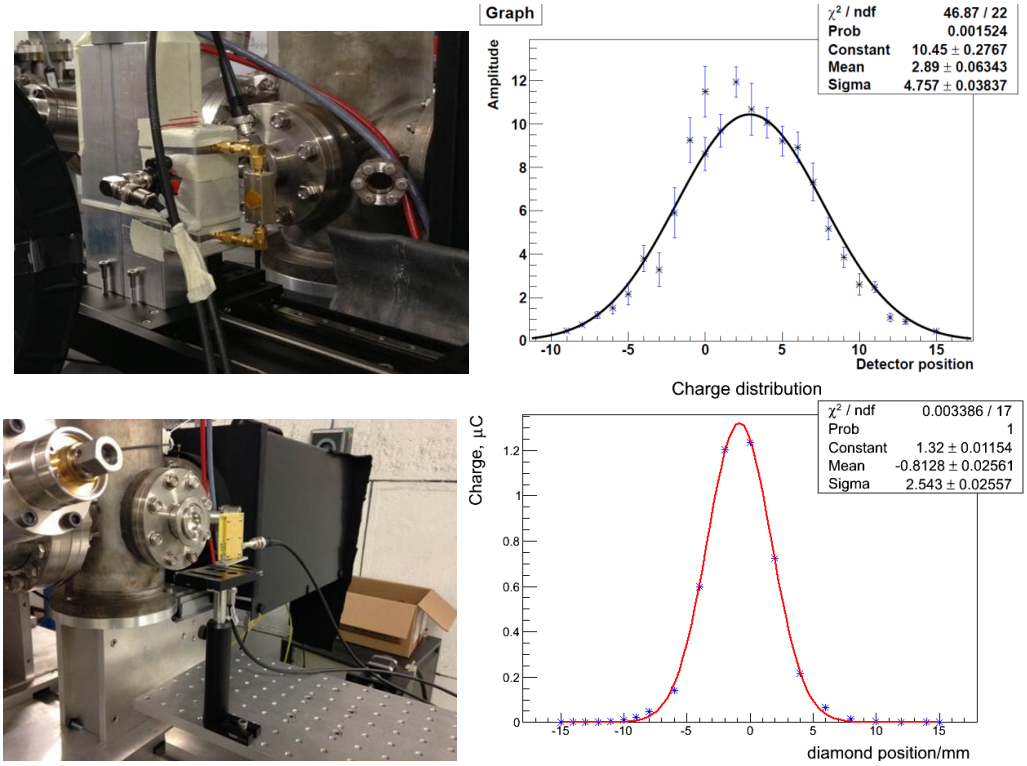

Figure 6.26: Beam size measurement using diamond sample No.1 (upper) and sample No.2 (bottom)

in Eq. 3.1, the effect of strip width on the beam size measurement can be taken into account by the following formula:

$$\sigma_{DS}^2 \approx \sigma_{fit}^2 - \left(\frac{d}{\sqrt{12}}\right)^2 \tag{6.20}$$

where d is the strip width, σ_{fit} is the beam size from the fit and σ_{DS} is the real measured beam size by DS. More detailed explanation about the signal convolution is given in Section 7.5.3.

The measurement set-up and results are presented in Fig. 6.26. The measurement conditions and beam size comparison with the YAG screen measured beam size are shown in Table 6.4. From this table it can be seen that the DS measured beam size is close to the YAG screen measured beam size (σ_{YAG}) only if the beam size is close to or bigger than the strip width, when the beam size is smaller, the measured beam size is larger than the real beam size.

	Distance to exit	σ_{YAG}	σ_{DS}
Sample No.1	10 cm	4.45±0.17 mm	4.57±0.04 mm
Sample No.2	3 cm	1.67±0.07 mm	2.19±0.03 mm

Table 6.4: Beam size measurement comparison

Therefore for the design of the in vacuum DS at ATF2, as the simulated beam size at DS location is around 1.5 mm, the strip width should not exceed 1.5 mm for the beam core measurement.